crystals

MDPI

Article

Biosynthesis Effect of Egg White on Formation and Characteristics of $NiO/NiCo_2O_4$ Nanocomposites

Ghadah M. Al-Senani [1], Foziah F. Al-Fawzan [1], Mashael Alshabanat [1], Omar H. Abd-Elkader [2,*], Mai Nasrallah [3] and Mohamed Nasrallah [4]

[1] Department of Chemistry, College of Science, Princess Nourah bint Abdulrahman University, P.O. Box 84428, Riyadh 11671, Saudi Arabia; ffalfozan@pnu.edu.sa (F.F.A.-F.)
[2] Physics and Astronomy Department, Science College, King Saud University, P.O. Box 2455, Riyadh 11451, Saudi Arabia
[3] Faculty of Medicine, Ain Shams University, El-Khalyfa El-Mamoun Street, Cairo 11774, Egypt
[4] Faculty of Medicine, Ibn Sina University, Aljerif West Block (88), Khartoum 11115, Sudan
* Correspondence: omabdelkader7@ksu.edu.sa

Abstract: For the successful production of $NiO/NiCo_2O_4$ nanocomposites, the environmentally friendly method of egg white supplementation has been used. Several analytical techniques were employed to characterize the morphology, purity, and crystal structure of the as-prepared nanocomposites. These techniques included transmission electron microscopy (TEM), Fourier-transform infrared spectroscopy (FTIR), scanning electron microscopy (SEM), and X-ray diffraction (XRD). The physical adsorption and magnetic properties of the investigated composite were determined using the Brunauer–Emmett–Teller (BET) method and a vibrating-sample magnetometer (VSM), respectively. The results have shown that the as-prepared composite particles had diameters of about 10–25 nm, with uniform distribution. The XRD analysis showed that the as-synthesized composites consisted entirely of cubic structures of both NiO and spinel $NiCo_2O_4$ nanoparticles, with a space group of Fd3m. The FTIR analysis showed characteristic vibration modes related to metal oxides, confirming the formation of composites containing NiO and $NiCo_2O_4$ crystallites. The investigated composites' saturation magnetization (M_S) and coercivity (H_C) were easily controllable because of the ingredients' ferromagnetic ($NiCo_2O_4$) and antiferromagnetic (NiO) characteristics. The excellent combination of the $NiO/NiCo_2O_4$ nanocomposites' properties is anticipated to make this system suitable for a wide range of applications.

Keywords: $NiO/NiCo_2O_4$ nanocomposites; spinel structural; vibration modes; superior performance; energy storage and supercapacitor

check for updates

Citation: Al-Senani, G.M.; Al-Fawzan, F.F.; Alshabanat, M.; Abd-Elkader, O.H.; Nasrallah, M.; Nasrallah, M. Biosynthesis Effect of Egg White on Formation and Characteristics of $NiO/NiCo_2O_4$ Nanocomposites. *Crystals* **2023**, *13*, 1579. https://doi.org/10.3390/cryst13111579

Academic Editor: Małgorzata Hołyńska

Received: 30 August 2023
Revised: 3 November 2023
Accepted: 6 November 2023
Published: 9 November 2023

Copyright: © 2023 by the authors. Licensee MDPI, Basel, Switzerland. This article is an open access article distributed under the terms and conditions of the Creative Commons Attribution (CC BY) license (https://creativecommons.org/licenses/by/4.0/).

1. Introduction

One major practical issue and problem is the deliberate development of polymetallic oxides, regardless of their use in electrical energy storage devices, such as lithium-ion batteries (LIBs) and electrochemical supercapacitors (SCs), with a unique micro-nano structure and shape. The primary objective of this assignment is to progress forward RuO_2, which is the predominant electrode material in supercapacitors, due to its prohibitive price and toxic effects on the environment [1]. One of the binary metal oxides, nickel cobaltite ($NiCo_2O_4$), has attracted considerable attention in energy conversion/storage systems, depending upon the unique characteristics of this cobaltite. In fact, $NiCo_2O_4$ has exceptional electrochemical capabilities, a variety of ions are involved in its rich redox processes, it contains complicated chemical elements, and it has the synergistic effects of multiple metal composition [2]. In other words, nickel cobaltite has electro-catalytic activity, a high electronic performance, and a capacitive performance higher than that of single NiO, Co_3O_4, and the noble metal oxide RuO_2. These advantages could be explained by the solid-phase redox couples of Co^{2+}/Co^{3+} and Ni^{2+}/Ni^{3+} in the cobaltite systems. Therefore,

cobaltite is employed in a broad range of applications, covering ferrofluid innovations, magnetic materials, electro catalysts, batteries powered by lithium ions, supercapacitors, and photodetectors [2,3]. On the reverse side, cobaltite materials are thought to be the most promising substitute material, due to their numerous advantages, such as their affordability, an unlimited supply of resources, environmental friendliness, etc., [4,5].

Compounds containing nickel and cobaltite have been produced using a variety of methods, such as sol-gel, coprecipitation, electrodeposition, microwave, and hydrothermal approaches [6–9]. These techniques have produced nanostructured $NiCo_2O_4$ in a variety of sizes and shapes [10–15]. For instance, Cheng et al. reported the preparation of $NiO/NiCo_2O_4$ composites with a unique yolk–shell structure using a simple hydrothermal route, followed by annealing at a high temperature [16]. $NiO/NiCo_2O_4$ nanocomposite was also prepared using a simple and eco-friendly method employing Urtica extract, followed by heating at a high temperature for the determination of dopamine [17]. A hetero-structure, necklace-like $NiO–NiCo_2O_4$ hybrid was prepared using a typical hydrothermal method for Li–oxygen batteries [18]. Exchange bias behaviors up to room temperature have been observed in a $NiCo_2O_4/NiO$ nanoparticle system prepared using the chemical co-precipitation method [19]. However, one of the problems encountered in most of the preparation procedures of cobaltite materials is a high calcination temperature and high crystallinity, with a subsequent decrease in the electrochemical activity and the specific capacitance of these materials. In this way, the challenge will be to develop the preparation of these materials. High purity, low grain size, a superior large specific surface area, and superior electrical conductivity can only be achieved through homogenous multicomponent metal oxide materials prepared using minimal-cost, lower-energy techniques. Even though there are other ways to create spinel $NiCo_2O_4$, the auto-combustion strategy is now regarded as one of the most attractive synthesis methods, due to its inherent advantages, which include homogenous heat transmission and an incredibly quick heating duration [20,21]. Utilizing combustion technology, rapid heating can be accomplished through efficient energy transmission. Furthermore, the homogenous heating of the precursor solution caused by auto-combustion or heating up enables the rapid achievement of a uniform distribution of particle size. Consequently, the auto-combustion method is more efficient than the conventional routes for preparing various oxide nanoparticles. The added value of this method increases when it relies on natural materials as fuel in the combustion process. We describe in this study the synthesis of porous $NiO/NiCo_2O_4$ nanomaterials utilizing a replication of the egg-white-assisted combustion technique, along with rapid air heating at 700 °C to remove all or some of the carbon ash generated during the combustion process.

The purpose of this work is to develop $NiO/NiCo_2O_4$ nanocomposites via the auto-combustion technique using egg white. Both XRD and FTIR methods are essential for the characterization of these composites. TEM/HRTEM, SEM, and EDS are used to identify the morphological and elemental properties of these composites. The produced composites' surface and magnetic characteristics are also investigated.

2. Materials and Methods

2.1. Materials

Cobalt (II) nitrate hexahydrate and nickel (II) nitrate hexahydrate were provided by Sigma-Aldrich Company and have the linear formulas of Co $(NO_3)_2$ $6H_2O$ and Ni $(NO_3)_2$ $6H_2O$, respectively. This analytical-grade reagent was utilized directly without further purification. The egg white was taken directly from a local hen's egg.

2.2. Preparation of Nanocomposite

The cobalt and nickel nitrates were combined with 5 mL of egg white to create a single sample of $NiO/NiCo_2O_4$. The combined precursors were concentrated for a quarter-hour at 300 °C in a porcelain crucible on a hot plate. The crystal water gradually evaporated, leaving behind a dense, frothy material in the container containing the virgin, or uncalcined,

sample (S1). To create the calcined sample (S2), the resultant solid was calcined in the air for an hour at 700 °C. A schematic representation of the synthesis of the samples containing $NiO/NiCo_2O_4$ nanoparticles is provided in Figure 1.

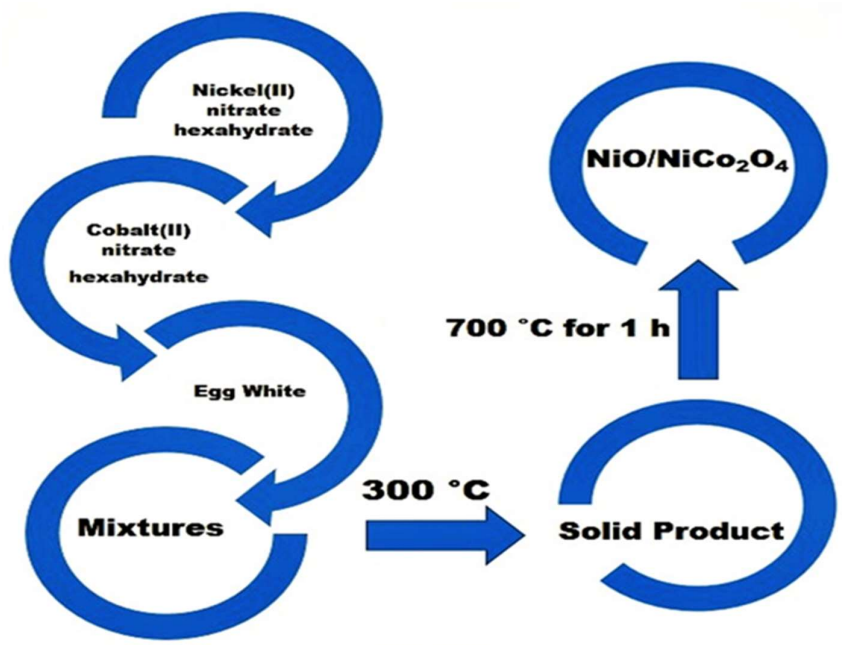


Figure 1. Schematic diagram of the fabrication process.

2.3. Characterization of Nanocomposite

Using a sophisticated diffractometer (BRUKER D8 from Bremen, Germany), several mixed solids were measured with X-rays. Cu Kα radiation was used to perform the patterns in 2θ at 40 kV and 40 mA, scanning at a speed of 2° min^{-1}.

On the basis of the computations of X-ray diffraction pattern broadening using the Scherer equation, the crystallite dimensions of the crystalline phases that comprise the substances under investigation have been established [22], as follows:

$$d = \frac{B\lambda}{\beta \cos \theta} \quad (1)$$

where the Bragg's angle is θ, the full-width-half-maximum (FWHM) of diffraction is β, the Scherrer constant (0.89) is B, the average crystallite size of the phase under study is d, and the wavelength of the X-ray beam utilized is λ.

A Perkin-Elmer spectrophotometer (type 1430), (Beaconsfield, UK) was used to measure the infrared transmission spectra of several materials. A total of 2 mg of each solid sample was combined with 200 mg of vacuum-dried IR-grade KBr, and the IR spectra were collected between 4000 and 400 cm^{-1}. The blend was worked for three minutes in a vibrating ball mill and then put into a 13-mm-diameter steel die under 12 tons of pressure. The double-grating infrared spectrometer's holder was filled with sample discs.

Following a brief exposure with ultrasonic treatment to disperse individual particles over copper grids, the samples were mounted for observations using transmittance electron micrographs (TEM) and scanning electron microscopes (SEM) (JEOL, Tokyo, Japan). EDS was performed using a JED-2200 Series electron microscope (JEOL, Tokyo, Japan), configured with Delta Kevex equipment. As operational parameters, we employed 6 µm window width, 120 s accumulation duration, and 20 kV accelerating voltage. The surface molar composition was calculated using the Asa method, Zaf correction, and Gaussian approximation.

Using the Brunauer–Emmett–Teller method and surface area analyzers from Micrometrics' Gemini VII 2390 V1.03 series, the surface area (S_{BET}), total pore volume (V_P), and

mean pore radius (r̂) of the as-prepared materials were determined. Before the measurements, each sample was out-gassed for 2 h at 200 °C at a reduced pressure of 10^{-5} Torr.

The magnetic characteristics of the evaluated substances were investigated using a vibrating-sample magnetometer (VSM; 9600-1 LDJ, Troy, MI, USA) with an optimal induced magnetic field of 20 kOe.

3. Results

3.1. XRD Study

A preliminary investigation based on X-ray analysis revealed that a virgin sample that had not been treated with egg white possessed an amorphous feature. The NiO/$NiCo_2O_4$-NPs-containing S1 and S2 XRD patterns are presented in Figure 2. The indexing planes (220), (311), (222), (400), (422), (333), (440), and (533) are represented by the peaks in these patterns. These peaks at 2θ values are 31.24°, 36.80°, 38.51°, 44.76°, 55.59°, 59.29°, 65.16°, and 77.25°, respectively. These correspond to the reported values for $NiCo_2O_4$ NPs (PDF No. 73-1702). For $NiCo_2O_4$ (major phase), all of the diffraction peaks can be indexed as having a typical cubic spinel structure. On the other hand, at degree 2θ = 37.03, 43.02, 62.48, 74.91, and 78.80, respectively, there is another set of diffraction peaks that are indicative of the indexing planes (111), (200), (220), (311), and (222), respectively. This is consistent with the NiO NPs stated values (PDF No. 78-0429). For NiO, the conventional cubic structure may be indexed for all of the diffraction peaks. The examined solid's XRD patterns showed no evidence of any other phases. Increasing the calcination temperature to 700 °C resulted in a rise in the peak height of the $NiCo_2O_4$ NPs and a decrease in that of the NiO NPs, indicating an increase in the nickel cobaltite.

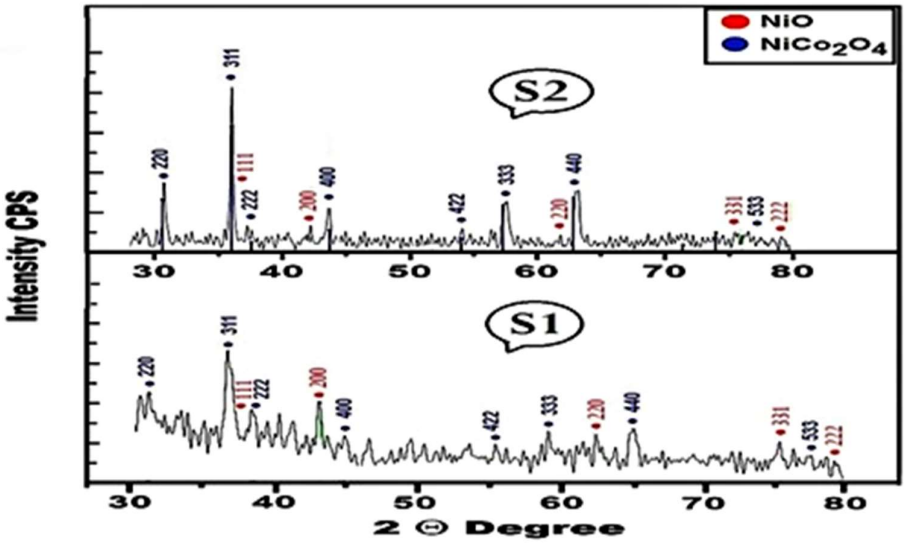


Figure 2. XRD patterns of the S1 and S2 samples.

As a result, the XRD results validate the formation of NiO/$NiCo_2O_4$ nanocomposites and reveal that the majority of the peaks in the XRD patterns are connected with the $NiCo_2O_4$ phase, which contains a percentage of cubic NiO. Based on the height of the particular diffraction peaks of NiO (200) and $NiCo_2O_4$ (311), the relative content or estimated fraction (F) of the NiO phase in the porous NiO/$NiCo_2O_4$ nanocomposite may be determined by applying the following relation:

$$F = I_{cubic}/I_{total} \quad (2)$$

where I_{total} equals the sum of the counts of $I_{(311)}$ and $I_{(200)}$, respectively, for the $NiCo_2O_4$ and NiO phases, and I_{cubic} is the count of $I_{(200)}$ of the cubic NiO phase. It was discovered that 33 and 10% of the cubic NiO phase was present prior to synthesis in the S1 and S2 samples containing porous NiO/$NiCo_2O_4$ nanocomposite, respectivley. Table 1 shows

the parameters of the crystallite size (d), the unit cell volume (V), the X-ray density (D_x), the lattice constants (a), and the dislocation density (δ). This table shows that applying a heat treatment at 700 °C, as seen in the S2 sample, causes the values of a, d, and V to increase, while the values of D_x and δ in the $NiCo_2O_4$ NPs drop. The opposite behavior was observed in these values for the NiO crystallites. Table 2 lists the other structural characteristics of the $NiCo_2O_4$ as it was produced. Depending on the XRD results, other structural properties of the $NiCo_2O_4$ NPs were calculated, including the distance between the magnetic ions (L_A and L_B), the ionic radii (r_A, r_B), and the bond lengths (A–O and B–O) on tetrahedral (A) and octahedral (B) sites [20–23]. As shown in Table 2, by heating the virgin sample at 700 °C, the values of L_A, L_B, r_A, r_B, A–O, and B–O increase.

Table 1. Some structural properties of the S1 and S2 samples containing $NiCo_2O_4$ and NiO.

Properties	S1		S2	
	$NiCo_2O_4$	NiO	$NiCo_2O_4$	NiO
Crystal structure	Cubic	Cubic	Cubic	Cubic
Lattice constant (a), nm	0.8087	0.4181	0.8375	0.4082
Unit cell volume (V) nm^3	0.5289	0.0731	0.5874	0.0680
Density, g/cm^3	6.040	6.10	5.4385	6.56
Dislocation density (δ)	2.770×10^{-3}	6.944×10^{-3}	1.372×10^{-3}	1.562×10^{-3}
Crystallite size (d), nm	19	12	27	8

Table 2. Other structural properties of $NiCo_2O_4$ NPs involved in the S1 and S2 samples.

Parameters	S1	S2
L_A	0.3502	0.3626
L_B	0.2858	0.2956
A–O	0.1849	0.1914
B–O	0.2086	0.2161
r_A	0.0244	0.0594
r_B	0.0275	0.0841

3.2. Fourier-Transform Infrared Spectroscopy (FTIR) Analysis

The FTIR spectral analysis of the NiO/$NiCo_2O_4$ ranging from 4000 to 400 cm^{-1} is presented in Figure 3. The vfrious ordering positions on the structural characteristics of the synthesized composites, and their locations in the crystal structure, are revealed by the spectra. The space group of cobaltites is usually Fd3m, and its crystal structure is spinel. The group theoretical calculations have revealed that the vibration spectra of the spinel cobaltites show the following two basic infrared active modes: a high frequency band (ν1) at around 600 cm^{-1} is the tetrahedral (A) site and a low frequency band (ν2) at about 422 cm^{-1} is the octahedral (B) site. The synthesized cobaltite's absorption bands in this investigation fall within the predicted range. The absorption bands are visible at 3343.4, 1613.9, 1351.8, 1102.7, 826.4, 649.6, 550.3, 422, and 415.5 cm^{-1} in the NiO/$NiCo_2O_4$ nanoparticles. According to Waldron [24], the high frequency band ν_1 at around 550.3 cm^{-1} and the low frequency band ν_2 at around 415.5 cm^{-1} are attributed to that of tetrahedral and octahedral complexes of the spinel structure, respectively. New bands ν_1* and ν_2* at 535 and 415.5 cm^{-1} are assigned to the divalent tetrahedral/octahedral metal ions and the oxygen ion complexes, respectively. However, the existence of strong bands at 698 and 826.4 cm^{-1} indicates the presence of NiO [25,26]. The numerous vibrational modes of the carbon groups, on the other hand, are responsible for the bands at 1102.3 and 1351.8 cm^{-1}. These bands are attributed to the C–O, C–OH, and/or C–H bonds' stretching vibrations [21]. A broad band at 1613.9 cm^{-1}, which indicates the presence of a hydroxyl group on the surface of the metal ions, indicates O–H bond stretching vibrations. The band at 3343.4 cm^{-1} may possibly be connected to a common band attributed to the bending

manner of the absorbed water as moisture, which disappears due to heating at 700 °C, as shown in the S2 sample [21].

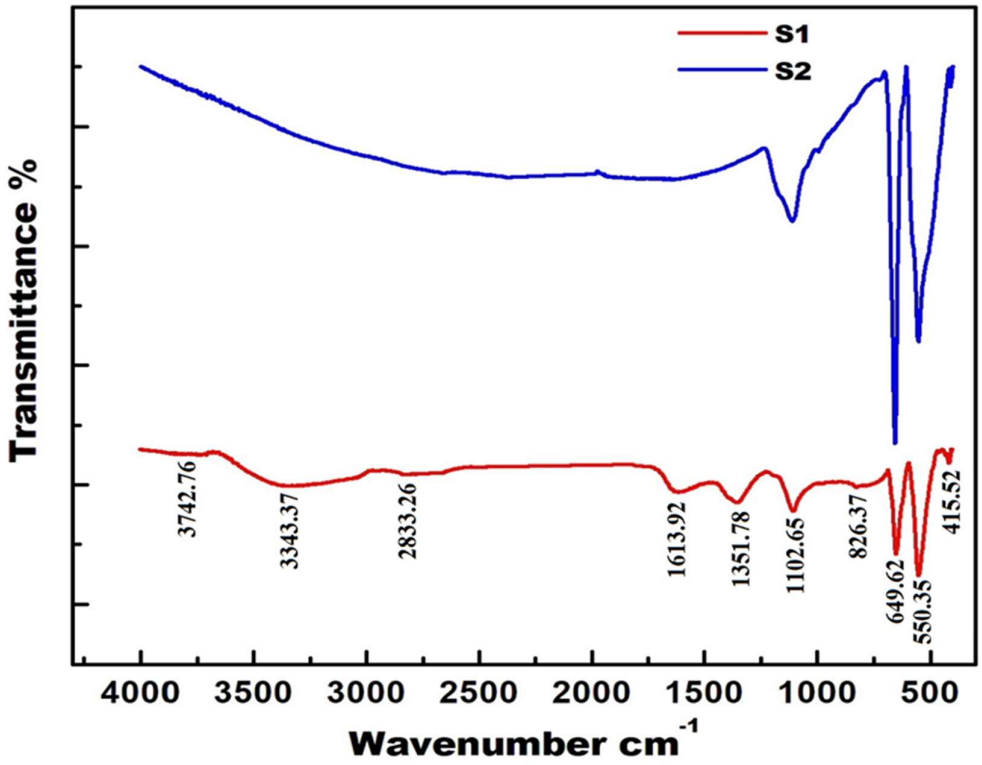


Figure 3. FTIR spectra of $NiO/NiCo_2O_4$ nanoparticles.

3.3. Morphological Characteristics of the Investigated Composite

The morphology of the synthesized $NiO/NiCo_2O_4$ was determined by using the SEM and TEM analyses, as shown in Figures 4 and 5, respectively. These analyses led to the study of some of the morphological properties, including the shape and size of particles, as well as the extent of their distribution or aggregation.

According to the SEM images shown in Figure 4a,b, the freshly prepared composites (S1 and S2) are primarily constructed of spherical and cube nanoparticles. The S1 sample contains spherical nanoparticles with dimensions ranging from 8 to 19 nm, which are clearly indications of a loosely packed porosity structure. We can characterize the S1 sample with having a sheet structure and a delicate, spongy appearance. Nonetheless, the porous structure and interaction space between the $NiO/NiCo_2O_4$ nanoparticles aid the improvement of the specific surface area by improving ion transport, reducing electron migration, and maintaining chemical stability. In contrast, the SEM picture for the S2 sample shows cube particles interspersed with some spherical particles, with an overall average size of 27 nm. These outcomes agree with the XRD analysis. On the other hand, several agglomerations in the S1 and S2 samples also showed a higher tendency. In fact, the majority of the manufactured composites' attributes, including their surface and magnetic qualities, will change due to the evident morphological changes brought about by the heat treatment.

By performing a chemical characterization and an elemental analysis of the $NiO/NiCo_2O_4$ composite, the EDS analysis was able to reveal more about the topography of this composite. Figure 4c,d display the synthesized samples' EDS patterns. The studied composite's total composition of Ni, Co, C, and O components is confirmed in this figure. These results are in strong accord with the XRD and FTIR results, which support the successful creation of the $NiO/NiCo_2O_4$ system.

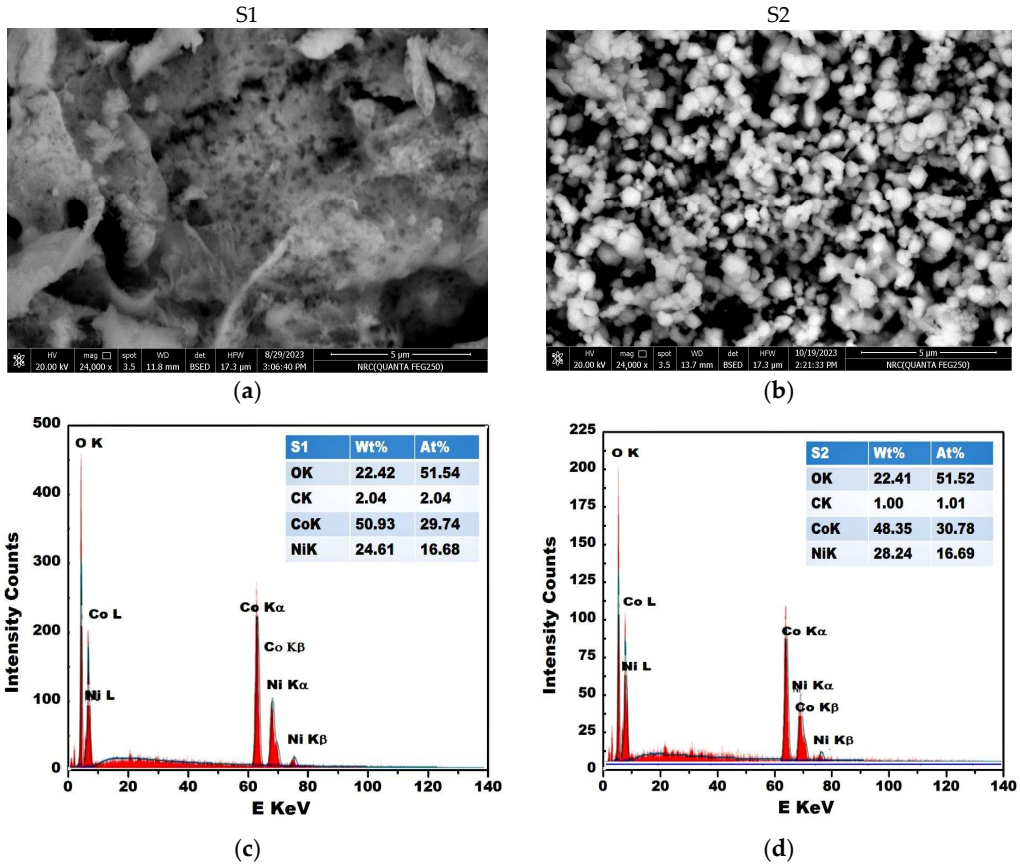


Figure 4. SEM images (**a**,**b**) and EDS pattern (**c**,**d**) of $NiO/NiCo_2O_4$ nanoparticles.

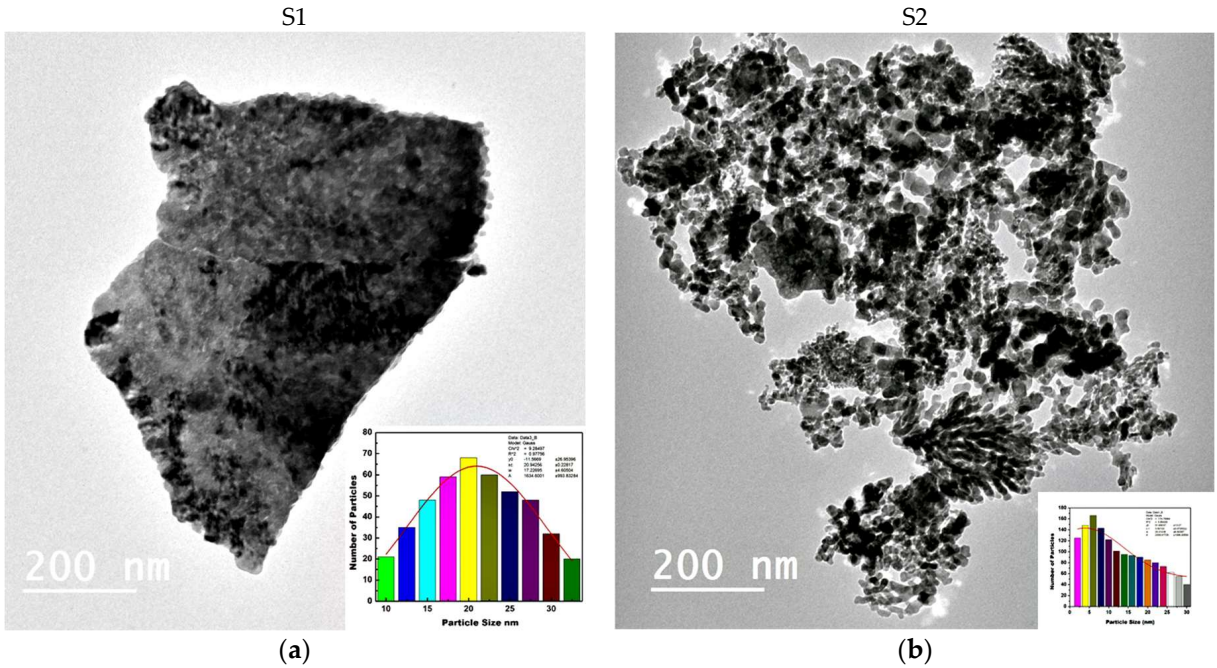
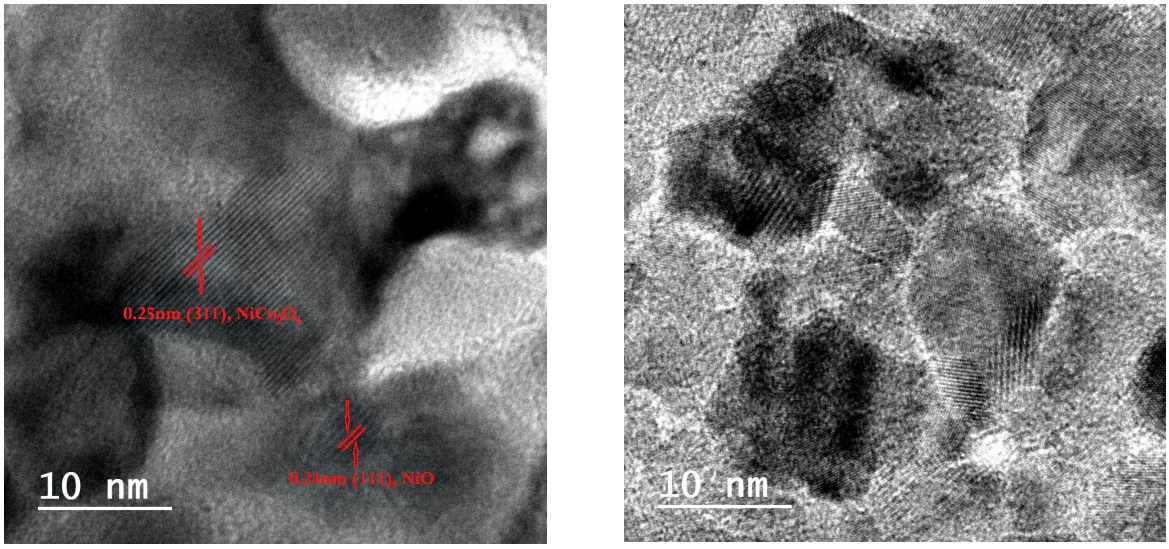


Figure 5. *Cont.*



(**c**) (**d**)

Figure 5. TEM images (**a**,**b**) and HR-TEM image (**c**,**d**) of the S1 and S2 samples.

The TEM photographs of the S1 and S2 samples are displayed in Figure 5a,b. These images verify that neither the S1 nor the S2 samples contain any homogeneous particles with varying nano sizes in the 8–30 nm range. The results of the SEM and the XRD corroborate with these observations. However, these composites exhibit interconnected pseudo-spherical particles or cubic particles, with the elongated nano array structures having edges with low crystallinity. The as-prepared composite nanostructure was examined with high-resolution TEM (HR-TEM) images (Figure 5c,d) in order to analyze the deep morphological characteristics and to calculate the atomic d-spacing. According to (PDF Numbers. 78-0429 and 73-1702), the d-spacing for the (111) and (311) orientations of the NiO and $NiCo_2O_4$ crystallites, respectively, was calculated using the fringes seen in the HR-TEM images of the nanocomposites. The result was 0.24 nm, which is extremely close to the theoretical d-spacing.

3.4. Surface Properties of NiO/$NiCo_2O_4$ Nanocomposites

Studying the surface properties of the produced samples is necessary in order to demonstrate that they are composed of porous materials. Therefore, as seen in Figure 6, the surface characteristics of the S1 and S2 nanocomposites were investigated by employing N_2 adsorption/desorption isotherms at −196 °C. These isotherms enabled us to determine the different surface properties of the studied samples, as shown in Table 3. After examining these isotherms, it was found that they belong to type-II, with a type H3 hysteresis loop, according to the IUPAC classifications [27]. In addition, these isotherms confirm that the used preparation method resulted in the formation of mesoporous nanocomposites. Additionally, based on the change in the adsorption process at a high relative pressure (P/Po = 0.83–0.98), we can deduce from the shape of the isotherm that a condensation process in the inter-particle voids occurred in the S2 sample. Moreover, one cannot ignore the fact that the S1 samples contain microspores, depending upon another jump in the adsorption process at a low relative pressure (P/P_o = 0.05), with a subsequent low slope region. Furthermore, the SEM and TEM investigations reveal the presence of plate-like particles or slit-like pores in the form of the H3 hysteresis loop. With the help of the non-local density functional theory (NLDFT) for the adsorption of nitrogen in the pores, we were able to obtain the pore distribution patterns at a pore scale for the different porous media (S1 and S2), as shown in Figure 6. We applied pore scale modeling to predict the underlying model of the pore space, which is representative of the pore structure, where the curves contained one model centered at 5 nm and another at 13 nm for the S1

and S2 samples, respectively. This result displays that the resulting nanocomposites are mesoporous materials. However, the heat treatment at 700 °C resulted in an increase in the pore size from 5 nm to 13 nm, indicating the formation of wedding pores. These findings confirm a decrease in the values of S_{BET}, V_m, and V_p for the S2 sample, compared to the S1 sample, as shown in Table 3.

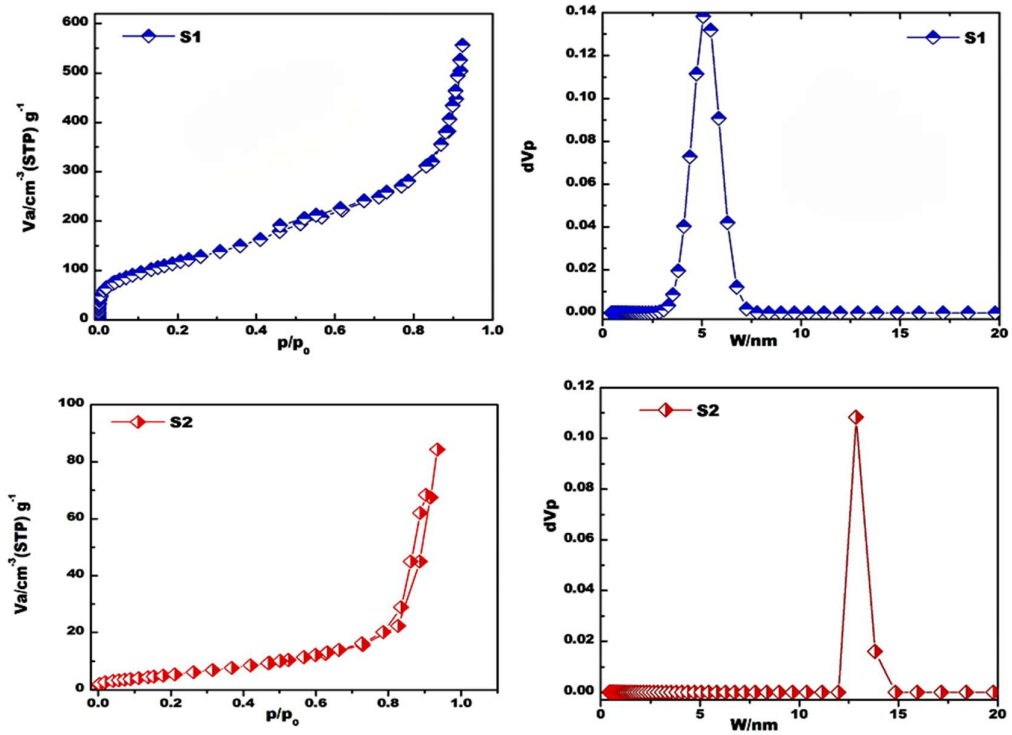


Figure 6. N_2 adsorption–desorption isotherms and pore size distribution of the S1 and S2 samples.

Table 3. Surface properties of the S1 and S2 samples.

Samples	SBET (m^2/g)	Vm (cc/g)	Vp (cc/g)	r̂(nm)
S1	24	5.479	0.1303	21.85
S2	18	4.136	0.0665	14.78

3.5. Magnetic Properties of NiO/$NiCo_2O_4$ Nanocomposites

By applying a magnetic field within the range of ±20 kOe at room temperature, the magnetic characteristics of the S1 and S2 samples containing the NiO/$NiCo_2O_4$ nanocomposite were evaluated. These measurements led to obtaining the hysteresis loops that are shown in Figure 7. The hysteresis loop of the S2 sample is S-shaped, which is a definite sign of room-temperature ferromagnetism (RTFM). The loop of the S1 sample indicates the presence of paramagnetic behavior, with slight ferromagnetism. On the other hand, as Table 4 illustrates, we were able to estimate the varied values of the majority of the magnetic properties for the composite that was the subject of our investigation. These properties include the coercive field (H_c), the squareness (M_r/M_s), the saturation magnetization (M_s), and the anisotropy constant (K_a). It can be seen from this table that the values of M_s, M_r, M_r/M_s, H_c, and K_a are 21.27 emu/g, 6.45 emu/g, 0.303, 126.29 Oe, and 2741 erg/cm^3, respectively.

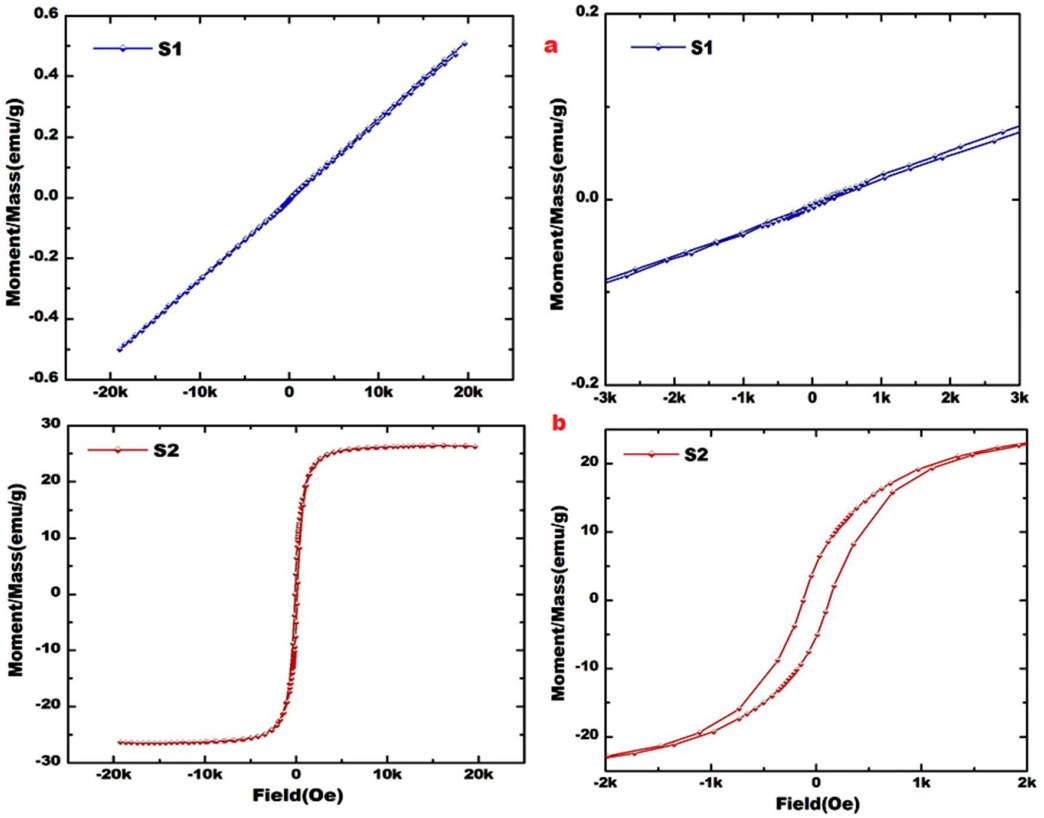


Figure 7. Magnetic properties of (**a**) the S1 sample and (**b**) the S2 sample.

Table 4. Magnetic properties of the as-synthesized $NiO/NiCo_2O_4$ nanocomposites.

Samples	M_s (emu/g)	M_r (emu/g)	M_r/M_s	H_c (Oe)	K_a (erg/cm^3)
S1	0.504	0.0024	0.0048	61	31
S2	21.27	6.45	0.303	126.29	2741

4. Discussion

4.1. Formation of Porous Nickel Cobaltite

The cobalt-oxide-based system is really composed of the following three well-known valence states: cobaltous oxide (CoO), cobaltic oxide (Co_2O_3), and cobalt cobaltite (Co_3O_4). In this system, the most stable phase is a mixed-valence molecule [$Co^{2+}Co_2{}^{3+}O_4$] with a classic spinel structure [24]. We have indicated that the preliminary experiments based on the X-ray analysis of the virgin sample prepared without egg whites was amorphous. In this study, the solid-state reaction between the nickel and cobalt oxides using the egg-white-assisted combustion method resulted in the synthesis of a nano-crystalline composite containing NiO and $NiCo_2O_4$. This relates to the role of egg white in the stimulation of the solid-state reaction between the amorphous cobalt and the nickel oxides, yielding $NiCo_2O_4$. Nonetheless, egg white plays a crucial role in the NiO nanoparticles' crystallization. The XRD and SEM results indicated that the $NiO/NiCo_2O_4$ crystallite size ranged from 8 to 27 nm. It is evident from Table 1 that there is some dislocation in the particle crystal lattices of the NiO and $NiCo_2O_4$, respectively. An irregularity or crystallographic imperfection within a crystal structure is called a dislocation, and it has a significant impact on the characteristics of materials. The regular atomic array of a flawless crystal is distorted by this imperfection [26–29]. Conversely, the X-ray data enabled us to calculate the different structural characteristics of the cubic spinel $NiCo_2O_4$, as follows: the bond lengths (A–O and B–O) on the tetrahedral (A) sites and octahedral (B) sites, the ionic radii (r_A and r_B),

and the separation between the reacting ions (L_A and L_B). Table 2 presents the values of the different structural features of the $NiCo_2O_4$ [29].

NiO and Co_3O_4 can react in a solid state to produce nickel-oxide-substituted cobaltic oxide ($Ni_xCo_{3-x}O_4$) compounds. The thermal diffusion of Ni and Co cations through the early nickel cobaltite film, which coats the surfaces of the reacting oxide grains and serves as an energy barrier, is influenced by a number of factors. These factors are the precursor compounds, the preparation method, and the preparation conditions. The production of the solid solution is facilitated by the enhanced mobility of the cobalt and nickel cations caused by the dissolution of the nickel ions in the cobalt lattices, which, in turn, creates oxygen vacancies. Furthermore, oxygen transport between the two metal oxides is favored by the close coexistence of the NiO and CoO_x crystallites. This type of NiO/CoO_x structure interaction led to an increase in the formation of the Co_2O_3 phase. This indicates the presence of a synergistic mechanism between the nickel and cobalt oxides. The proposed mechanism in this case is as follows:

$$3Co_2O_3 \rightarrow 2Co_3O_4 + 1/2\ O_2 \quad (3)$$

$$2Co_3O_4 + 2Ni^{2+} \rightarrow 2NiCo_2O_4 + 2Co^{2+} \quad (4)$$

$$2Co^{2+} + 3NiO + 1/2\ O_2 \rightarrow NiCo_2O_4 + 2Ni^{2+} \quad (5)$$

Alternatively, the $NiCo_2O_4$ particles were created as a result of the counter-diffusion of Ni^{2+} and Co^{3+} through a cobaltite layer that was comparatively stiff [30]. Considering that we have detected Co^{2+} at the interface, we hypothesize that the diffusing ions may also include Co^{3+}. Additionally, the subsequent reactions show that, at the Co_2O_3 interface, the Co_2O_3 breaks down into $2Co^{2+}$ and oxygen gas. Additionally, oxygen diffuses through the reaction zone to interact with the NiO interface in order to create a spinel structure by interacting with Co^{2+} and NiO, as follows:

At the Co_2O_3 interface:

$$3Co_2O_3 + 2Ni^{2+} \rightarrow 2NiCo_2O_4 + 2Co^{2+} + 1/2\ O_2 \quad (6)$$

At the NiO interface:

$$2Co^{2+} + 3NiO + 1/2\ O_2 \rightarrow NiCo_2O_4 + 2Ni^{2+} \quad (7)$$

Egg white has received much attention due to its gelling, foaming, and emulsifying characteristics, which facilitate the solubility of inorganic materials. It is less expensive, readily available, ecologically friendly, and cost-effective. It is also a biological liquid with a high carbohydrate and protein content, including albumin, which serves as a bio-template [31,32]. The proteins can interact with inorganic nanoparticles and then govern the nucleation of the inorganic materials in aqueous solutions. Therefore, egg white can be used as a sol stabilizer, an egg-gelled flame fuel, and a growth-control agent for the production of nanoparticles [33]. Generally, egg white can be employed for the production of different nanomaterials with controlled morphology.

In this study, the formation process of $NiCo_2O_4$ crystallites with the assistance of egg white can be tentatively proposed. During the reaction, the Ni^{2+} and Co^{2+} ions react with the egg albumin to form a complex; moreover, the combination of the nitrogen atoms in the egg albumin molecules and both the Ni^{2+} and Co^{2+} ions can promote aggregate growth. Due to the stacking interactions and the crystal packing force, the aggregates prefer to grow into a flake structure. If the amount of egg albumin is sufficient, the flakes tend to be stacked, owing to the existence of hydrogen bonds among the molecules, leading to the formation of final layered sphere and cube structures, as shown in the SEM images for the S1 and S2 samples, respectively [34]. The same mechanism occurs to form NiO crystals, so that we end up with mesoporous $NiO/NiCo_2O_4$ composites with a surface area of 18 and 24 m^2/g.

4.2. Cation Distribution

The increasingly finer spectral features of the surface atoms in the nanostructured materials suggest that their FTIR spectra will differ significantly from those of their coarse-grained polycrystalline and single-crystalline equivalents [35,36]. The broadness of the absorption bands indicates that the NiO and $NiCo_2O_4$ powders are nanocrystals. The size of the NiO/$NiCo_2O_4$ nanoparticles used in this study ranged between 8 and 27 nm. The tetrahedral position of the Ni–O and Co–O complexes differs from the octahedral position, due to the lower mass and charge of the Ni^{2+} ions compared to that of both the Co^{2+} and Co^{3+} ions. Moreover, there are spatial variations in the cation–oxygen bond strength (cation–oxygen force constant) [37]. The absorption band corresponding to the tetrahedral complexes, ν_1, which consists of sub-bands ν_1*, centered at ~550.3 cm^{-1}, and ν_1**, centered at ~535 cm^{-1}, was detected. However, the octahedral region contains two bands at ~422 cm^{-1} and ν_2* ~415.5 cm^{-1}. The splitting of the octahedral or tetrahedral IR absorption bands is due to the large difference in the reduced mass of both the octahedral (Ni^{2+} and Co^{3+}) complexes and the tetrahedral ($Ni^{2+}$and Co^{3+}) complexes. If only the Co^{3+} ions had been present at the octahedral site, the octahedral band would have been single. Similar results were observed in the nickel cobaltite system prepared by using the coprecipitation method [38].

The tetrahedral (B) sites have been inhabited preferentially by the Ni^{2+} ions, whereas the tetrahedral (A) and octahedral (B) sites have been occupied preferentially by the Co^{3+} ions [30,39]. When the spinel is normal, the parameter of inversion, x, equals 1, and when it is inverse, it equals 0. The inverse spinel distribution of the $NiCo_2O_4$ is, therefore, perfect, as follows:

$$(Co_x{}^{3+})_A[Ni_{1-y}{}^{2+}\ Co_{1-x}{}^{3+}]_BO_4{}^{2-} \quad (8)$$

However, the findings in this study confirm the migration of some of the Ni^{2+} ions from the octahedral (B) sites to the tetrahedral (B) sites, with the following speculated formula:

$$(Ni_y{}^{2+}\ Co_x{}^{3+})_A[Ni_{1-y}{}^{2+}\ Co_{1-x}{}^{3+}]_BO_4{}^{2-} \quad (9)$$

This indicates that the as-prepared nickel cobaltite has a partially inverse or random spinel structure. This depends upon the preparation method and the coexistence of NiO with $NiCo_2O_4$. The data shown in Table 2 confirm this speculation, depending upon the decrease in the values of r_A and A–O. This indicates that the concentration of the nickel and cobalt ions at the (B) site is greater than that at the (A) site.

In fact, the combination of the ferromagnetic (FM) and antiferromagnetic (AFM) phases allows for a tuning of both the M_S and the H_C of the different composites [40]. However, various studies have reported that the individual cobalt and nickel oxides are typical of an AFM material, in which the magnetization increases almost linearly with the magnetic field [41]. Conversely, due to its FM nature, the solid–solid interaction between the Co and Ni oxides that results in the spinel $NiCo_2O_4$ phase frequently improves the composites' hysteresis loop. Similar investigations have revealed that the mesoporous pure $NiCo_2O_4$ (26 emu/g) has a higher M_S than the Ni–Co oxides composite, which contains 30 weight percent NiO and 70 weight percent $NiCo_2O_4$ [40,41]. That composite has an M_S of 17 emu/g. In this study, the investigated nanocomposite (S2) has an M_S of 21.27 emu/g, which is slightly lower than that of the bulk $NiCo_2O_4$ (29 emu/g) [42]. These authors have reported that the magnetic measurements are a powerful fingerprint of the presence of phases with dissimilar magnetic properties in the composites [43]. The coercivity of the investigated composites could be attributed to the following two main contributions (apart from magnetocrystalline anisotropy): shape anisotropy and AFM–FM exchange coupling. Since this is an interface effect, the amount of AFM material and the degree of coupling determine the coercivity enhancement [43]. Moreover, FM materials are known to have magnetic disorder at the surface, which depends on the shape, which also contributes to the H_C at low temperatures. The room temperature FM characteristic (RTFM) of the

investigated composite opens new perspectives for its applications in different fields, such as water treatment and heterogeneous catalysis.

The magnetic studies of the $NiO/NiCo_2O_4$ nanocomposite prepared in this study required shedding light on the magnetic properties of the individual oxides that make up this composite. These properties are evident from our previous work, therefore, this study is a continuation of what was studied in our research plan. Table 5 contains the magnetic properties of both the Ni/NiO and the Co/Co_3O_4 prepared from their respective nitrates using an egg-white-based combustion method [44,45]. It is clear from this table that the magnetism results of the Ni/NiO and Co/Co_3O_4 nanoparticles were 8.648 and 3.450 emu/g, respectively. Finally, the egg-white-assisted auto-combustion method, followed by heating at 700 °C, resulted in the enhancement of the magnetic properties of the S2 sample, compared with the uncalcined, S1, sample.

Table 5. Magnetic properties of some individual metal oxides that were studied in our previous works.

Samples	M_s (emu/g)	M_r (emu/g)	M_r/M_s	H_c (Oe)	K_a (erg/cm^3)	Reference No.
Ni/NiO	8.648	1.290	0.149	39.639	310.79	[44]
Co/Co_3O_4	3.450	0.273	0.079	85.032	299.35	[45]

5. Conclusions

For the first time, $NiO/NiCo_2O_4$ nanoparticles were created using a green synthesis process based on egg white. The synthesis of $NiO/NiCo_2O_4$ nanoparticles using this approach has various benefits, including economic feasibility, an ease of scaling up, and a reduced process time. According to the XRD measurements, the virgin (uncalcined) and calcined materials were fully composed of cubic NiO and $NiCo_2O_4$ phases at 700 °C. The SEM analysis indicates that the virgin composite was composed of many irregular and disordered spherical nanoparticles, with a polycrystalline structure. The image of the SEM for the calcined composite calcined at 700 °C shows the formation of nanoparticles with semispherical and cube-like structures. The EDS analysis confirms that the prepared composites consisted entirely of Ni, Co, O, and C elements. The used preparation method resulted in the formation of mesoporous composites with surface areas of 18 and 24 m^2/g. The magnetic characteristics of the $NiO/NiCo_2O_4$ composite calcined at 700 °C, namely the M_s, M_r, M_r/M_s, H_c, and K_a, were 21.27 emu/g, 6.45 emu/g, 0.303, 126.29 Oe, and 2741 erg/cm^3, respectively. Whereas the M_s, M_r, M_r/M_s, H_c, and K_a for the virgin composite were 0.504 emu/g, 0.0024 emu/g, 0.0048, 61 Oe, and 31 erg/cm^3, respectively.

Author Contributions: Conceptualization, O.H.A.-E., M.N. (Mai Nasrallah) and G.M.A.-S.; methodology, F.F.A.-F.; software, M.N. (Mohamed Nasrallah).; validation, O.H.A.-E., M.N. (Mai Nasrallah), M.A., and G.M.A.-S.; formal analysis, O.H.A.-E.; investigation, O.H.A.-E. and M.N. (Mohamed Nasrallah); resources, O.H.A.-E.; data curation, M.N. (Mai Nasrallah), and G.M.A.-S.; writing—original draft preparation, O.H.A.-E., G.M.A.-S., and M.A.; writing—review and editing, O.H.A.-E., G.M.A.-S., M.A. and M.N. (Mohamed Nasrallah); visualization, O.H.A.-E., G.M.A.-S., and M.N. (Mai Nasrallah); supervision, O.H.A.-E., M.A., and G.M.A.-S.; project administration, O.H.A.-E. and G.M.A.-S.; funding acquisition, G.M.A.-S., M.A., and F.F.A.-F. All authors have read and agreed to the published version of the manuscript.

Funding: This research was funded by the Princess Nourah bint Abdulrahman University Researchers Supporting Project Number: (PNURSP2023R67), Princess Nourah bint Abdulrahman University, Riyadh, Saudi Arabia.

Institutional Review Board Statement: Not applicable.

Informed Consent Statement: Not applicable.

Data Availability Statement: The data presented in this study are available on request from the corresponding author.

Acknowledgments: The authors are grateful to the support by Princess Nourah bint Abdulrahman University Researchers Supporting Project Number: (PNURSP2023R67), Princess Nourah bint Abdulrahman University, Riyadh, Saudi Arabia.

Conflicts of Interest: The authors declare no conflict of interest.

References

1. Liu, L.; Zhang, H.; Fang, L.; Mu, Y.; Wang, Y. Facile preparation of novel dandelion-like Fe-doped $NiCo_2O_4$ microspheres@ nanomeshes for excellent capacitive property in asymmetric supercapacitors. *J. Power Sources* **2016**, *327*, 135–144. [CrossRef]
2. Wang, C.; Zhou, E.; He, W.; Deng, X.; Huang, J.; Ding, M.; Wei, X.; Liu, X.; Xu, X. $NiCo_2O_4$-based supercapacitor nanomaterials. *Nanomaterials* **2017**, *7*, 41. [CrossRef] [PubMed]
3. Zhu, Y.; Pu, X.; Song, W.; Wu, Z.; Zhou, Z.; He, X.; Lu, F.; Jing, M.; Tang, B.; Ji, X. High capacity $NiCo_2O_4$ nanorods as electrode materials for supercapacitor. *J. Alloys Compd.* **2014**, *617*, 988–993. [CrossRef]
4. Gao, G.; Wu, H.B.; Ding, S.; Liu, L.M.; Lou, X.W. Hierarchical $NiCo_2O_4$ nanosheets grown on Ni nanofoam as high-performance electrodes for supercapacitors. *Small* **2015**, *11*, 804–808. [CrossRef]
5. Yang, M.; Chen, A.; Zhang, Y.; Le, L. Synthesis and characterization of Nano $NiCo_2O_4$ by microwave promoted precipitation method. *IOP Conf. Ser. Mater. Sci. Eng.* **2018**, *397*, 012087. [CrossRef]
6. Wu, Z.; Zhu, Y.; Ji, X. $NiCo_2O_4$-based materials for electrochemical supercapacitors. *J. Mater. Chem. A* **2014**, *2*, 14759–14772. [CrossRef]
7. Wang, N.; Sun, B.; Zhao, P.; Yao, M.; Hu, W.; Komarneni, S. Electrodeposition preparation of $NiCo_2O_4$ mesoporous film on ultrafine nickel wire for flexible asymmetric supercapacitors. *J. Chem. Eng.* **2018**, *345*, 31–38. [CrossRef]
8. Xiao, Y.; Lei, Y.; Zheng, B.; Gu, L.; Wang, Y.; Xiao, D. Rapid microwave-assisted fabrication of 3D cauliflower-like $NiCo_2S_4$ architectures for asymmetric supercapacitors. *RSC Adv.* **2015**, *5*, 21604–21613. [CrossRef]
9. Gao, S.; Liao, F.; Ma, S.; Zhu, L.; Shao, M. Network-like mesoporous $NiCo_2O_4$ grown on carbon cloth for high-performance pseudocapacitors. *J. Mater. Chem. A* **2015**, *3*, 16520–16527. [CrossRef]
10. Li, S.; Yang, K.; Ye, P.; Jiang, H.; Zhang, Z.; Huang, Q.; Wang, L. Hierarchical interpenetrating rHGO-decorated $NiCo_2O_4$ nanowires architectures for high-performance supercapacitors. *Appl. Surf. Sci.* **2019**, *473*, 326–333. [CrossRef]
11. Zhang, W.; Xin, W.; Hu, T.; Gong, Q.; Gao, T.; Zhou, G. One-step synthesis of $NiCo_2O_4$ nanorods and firework-shaped microspheres formed with necklace-like structure for supercapacitor materials. *Ceram. Int.* **2019**, *45*, 8406–8413. [CrossRef]
12. Luo, Y.; Guo, R.; Li, T.; Li, F.; Meng, L.; Yang, Z.; Wan, Y.; Luo, H. Conductive polypyrrole coated hollow $NiCo_2O_4$ microspheres as anode material with improved pseudocapacitive contribution and enhanced conductivity for lithium-ion batteries. *ChemElectroChem* **2019**, *6*, 690–699. [CrossRef]
13. Fan, H.L.; Zhang, J.; Ju, W.; Liu, B.X.; Zhao, X.F.; Liu, X.C.; Yi, X.B. Growth of $NiCo_2O_4$ nanotubes@ MnO_2 sheet core-shell arrays on 3D hierarchical porous carbon aerogels as superior electrodes for supercapacitors. *Int. J. Nanomanuf.* **2019**, *15*, 92–104. [CrossRef]
14. Li, D.; Li, Y.; Chen, R.; Ni, H. Direct synthesis of $NiCo_2O_4$ nanoneedles and MoS_2 nanoflakes grown on 316L stainless steel meshes by two step hydrothermal method for HER. *Acta Metall. Sin.* **2018**, *54*, 1179–1186.
15. Dai, J.; Zhao, R.; Xiang, J.; Wu, F.; Xin, L.; Zhang, Y.; Ma, S. Facile hydrothermal synthesis and their electrochemical performance of $NiCo_2O_4$ nanosheets. *Sci. Adv. Mater.* **2019**, *11*, 379–385. [CrossRef]
16. Cheng, X.; Zhou, X.; Wang, S.; Liu, Z.; Liu, Q.; Zhang, Y.; Liu, Q.; Li, B. Fabrication of $NiO/NiCo_2O_4$ Mixtures as Excellent Microwave Absorbers. *Nanoscale Res. Lett.* **2019**, *14*, 155. [CrossRef]
17. Amiri, M.; Javar, H.A.; Mahmoudi-Moghaddam, H. Facile Green Synthesis of $NiO/NiCo_2O_4$ Nanocomposite as an Efficient Electrochemical Platform for Determination of Dopamine. *Electroanalysis* **2021**, *33*, 1205–1214. [CrossRef]
18. Mohamed, Z.; Zhang, G.; He, B.; Fan, Y. Heterostructure Necklace-like NiO-$NiCo_2O_4$ Hybrid with Superior Catalytic Capability as Electrocatalyst for Li-Oxygen Batteries. *Eng. Sci.* **2021**, *17*, 231–241.
19. Zhu, C.M.; Wang, L.G.; Liu, F.C.; Kong, W.J. Exchange bias behaviors up to room temperature in $NiCo_2O_4/NiO$ nanoparticle system. *Ceram. Int.* **2019**, *45*, 9878–9883. [CrossRef]
20. Deraz, N. Construction of $Mn_{0.5}Mg_{0.5}Fe_2O_4$ Nano Particles. *Egypt. J. Chem.* **2018**, *61*, 531–538. [CrossRef]
21. Abd-Elkader, O.H.; Deraz, N.M.; Aleya, L. Rapid Bio-Assisted Synthesis and Magnetic Behavior of Zinc Oxide/Carbon Nanoparticles. *Crystals* **2023**, *13*, 1081. [CrossRef]
22. Cullity, B.D. *Elements of X-ray Diffraction*; Chapter 14; Addison-Wesley Publishing Co., Inc.: Boston, MA, USA, 1956.
23. Ganachari, S.V.; Bhat, R.; Deshpande, R.; Venkataraman, A. Synthesis and characterization of nickel oxide nanoparticles by self-propagating low temperature combustion method. *Recent Res. Sci. Technol.* **2012**, *4*, 4.
24. Waldron, R.D. Infrared spectra of ferrites. *Phys. Rev.* **1955**, *99*, 1727. [CrossRef]
25. Shinde, V.R.; Mahadik, S.B.; Gujar, T.P.; Lokhande, C.D. Supercapacitive cobalt oxide (Co_3O_4) thin films by spray pyrolysis. *Appl. Surf. Sci.* **2006**, *252*, 7487–7492. [CrossRef]
26. Rendale, M.K.; Mathad, S.N.; Puri, V. Thick films of magnesium zinc ferrite with lithium substitution: Structural characteristics. *Int. J. Self-Propagating High-Temp. Synth.* **2015**, *24*, 78–82. [CrossRef]

27. Baldovino-Medrano, V.G.; Niño-Celis, V.; Isaacs Giraldo, R. Systematic Analysis of the Nitrogen Adsorption–Desorption Isotherms Recorded for a Series of Materials Based on Microporous–Mesoporous Amorphous Aluminosilicates Using Classical Methods. *J. Chem. Eng. Data.* **2023**, *68*, 2512–2528. [CrossRef]
28. Mathad, S.N.; Jadhav, R.N.; Patil, N.D.; Puri, V. Structural and mechanical properties of Sr^{+2}-doped bismuth manganite thick films. *Int. J. Self-Propagating High-Temp. Synth.* **2013**, *22*, 180–184. [CrossRef]
29. Mathad, S.N.; Jadhav, R.N.; Phadtare, V.; Puri, V. Structural and mechanical properties of Sr-doped barium niobate thick films. *Int. J. Self-Propagating High-Temp. Synth.* **2014**, *23*, 145–150. [CrossRef]
30. Standley, K.J. *Oxide Magnetic Materials*; Oxford at Clarendon Press: London, UK, 1962; p. 24.
31. Rath, C.; Anand, S.; Das, R.P.; Sahu, K.K.; Kulkarni, S.D.; Date, S.K.; Mishra, N.C. Dependence on cation distribution of particle size, lattice parameter, and magnetic properties in nanosize Mn–Zn ferrite. *J. Appl. Phys.* **2002**, *91*, 2211–2215. [CrossRef]
32. Sudalai Muthu, K.; Perumal, P. Synthesis and characterization of NiO Nanoparticles using egg white method. *J. Mater. Sci. Mater. Electron.* **2017**, *28*, 9612–9617. [CrossRef]
33. Chang, C.; Meikle, T.G.; Su, Y.; Wang, X.; Dekiwadia, C.; Drummond, C.J.; Conn, C.E.; Yang, Y. Encapsulation in egg white protein nanoparticles protects antioxidant activity of curcumin. *Food Chem.* **2019**, *280*, 65–72. [CrossRef] [PubMed]
34. Kargar, H.; Ghazavi, H.; Darroudi, M. Size-controlled and bio-directed synthesis of ceria nanopowders and their in vitro cytotoxicity effects. *Ceram. Int.* **2015**, *41*, 4123–4128. [CrossRef]
35. Sun, J.; Wang, Y.; Zhang, Y.; Xu, C.; Chen, H. Egg albumin-assisted hydrothermal synthesis of Co_3O_4 quasi-cubes as superior electrode material for supercapacitors with excellent performances. *Nanoscale Res. Lett.* **2019**, *14*, 340. [CrossRef] [PubMed]
36. Abdulkhadar, M.; George, K.C. Study of laser Raman spectra of nanoparticles of AgI and HgI_2. *Solid State Commun.* **1992**, *84*, 603–606. [CrossRef]
37. Abdulkhadar, M.; Thomas, B. Raman scattering in nanoparticles of mercuric iodide. *Mater. Res. Bull.* **1995**, *30*, 1301–1308. [CrossRef]
38. Vivekanand, V.; Ryden, P.; Horn, S.J.; Tapp, H.S.; Wellner, N.; Eijsink, V.G.; Waldron, K.W. Impact of steam explosion on biogas production from rape straw in relation to changes in chemical composition. *Bioresour. Technol.* **2012**, *123*, 608–615. [CrossRef]
39. Ivanenko, I.; Voronova, A.; Astrelin, I.; Romanenko, Y. Structural and catalytic properties of Ni–Co spinel and its composites. *Bull. Mater. Sci.* **2019**, *42*, 172. [CrossRef]
40. Mohammed, E.M.; Malini, K.A.; Kurian, P.; Anantharaman, M.R. Modification of dielectric and mechanical properties of rubber ferrite composites containing manganese zinc ferrite. *Mater. Res. Bull.* **2002**, *37*, 753–768. [CrossRef]
41. Cabo, M.; Pellicer, E.; Rossinyol, E.; Estrader, M.; López-Ortega, A.; Nogués, J.; Castell, O.; Suriñach, S.; Baró, M.D. Synthesis of compositionally graded nanocast $NiO/NiCo_2O_4/Co_3O_4$ mesoporous composites with tunable magnetic properties. *J. Mater. Chem.* **2010**, *20*, 7021–7028. [CrossRef]
42. Cabo, M.; Pellicer, E.; Rossinyol, E.; Castell, O.; Surinach, S.; Baró, M.D. Mesoporous $NiCo_2O_4$ spinel: Influence of calcination temperature over phase purity and thermal stability. *Cryst. Growth Des.* **2009**, *9*, 4814–4821. [CrossRef]
43. Knop, O.; Reid, K.I.; Sutarno; Nakagawa, Y. Chalkogenides of the transition elements. VI. X-Ray, neutron, and magnetic investigation of the spinels Co_3O_4, $NiCo_2O_4$, Co_3S_4, and $NiCo_2S_4$. *Can. J. Chem.* **1968**, *46*, 3463–3476. [CrossRef]
44. Al-Senani, G.M.; Al-Fawzan, F.F.; Alshabanat, M.; Abd-Elkader, O.H.; Nasrallah, M.; Nasrallah, M. One pot synthesis, surface and magnetic properties of Ni-NiO@C composite. *Crystals* **2023**, *13*, 1497. [CrossRef]
45. Al-Senani, G.M.; Deraz, N.M.; Abd-Elkader, O.H. Magnetic and characterization studies of CoO/Co_3O_4 nanocomposite. *Processes* **2020**, *8*, 844. [CrossRef]

Disclaimer/Publisher's Note: The statements, opinions and data contained in all publications are solely those of the individual author(s) and contributor(s) and not of MDPI and/or the editor(s). MDPI and/or the editor(s) disclaim responsibility for any injury to people or property resulting from any ideas, methods, instructions or products referred to in the content.